



Article

Effect of MgFe-LDH with Reduction Pretreatment on the Catalytic Performance in Syngas to Light Olefins

Jie Li ¹, Changxiao Li ¹, Qiong Tang ¹, Zhijun Zuo ^{2,*}, Lei Liu ^{1,*}  and Jinxiang Dong ¹ 

¹ College of Chemical Engineering and Technology, Taiyuan University of Technology, Taiyuan 030024, China; lj19960323a@163.com (J.L.); lcx2940162749@163.com (C.L.)

² State Key Laboratory of Clean and Efficient Coal Utilization, Taiyuan University of Technology, Taiyuan 030024, China

* Correspondence: zuozhijun@tyut.edu.cn (Z.Z.); liulei@tyut.edu.cn (L.L.)

Abstract: MgFe-layered double hydroxides (LDH) were widely used as catalysts for Fischer–Tropsch synthesis to produce light olefins, in which the state of Fe-species may affect the resulting catalytic active sites. Herein, the typical MgFe-LDH was hydrothermally synthesized and the obtained MgFe-LDH was pretreated with H₂ at different temperatures to reveal the effects of the state of Fe-species on the catalytic performance in Fischer–Tropsch synthesis. MgFe-LDH materials were characterized by X-ray diffraction (XRD), N₂ adsorption–desorption, scanning electron microscopy (SEM), transmission electron microscopy (TEM), H₂ temperature-programmed reduction (H₂-TPR), and X-ray photoelectron spectroscopy (XPS). It was found that a MgO-FeO solid solution would be formed with the increase of the reduction temperature, which made the electrons transfer from Mg atoms to Fe atoms and strengthened the adsorption of CO. The pre-reduced treatment toward Mg-Fe-LDH enabled the FeC_x active sites to be easily formed in situ during the reaction process, leading to the high conversion of CO. CO₂ temperature-programmed desorption (CO₂-TPD) and H₂ temperature-programmed desorption (H₂-TPD) analysis confirmed that the surface basicity of the catalysts was increased and the hydrogenation capacity was weakened, the secondary hydrogenation of the olefins was inhibited, and therefore as were the enhancement of O/P in the product and the high selectivity of light olefins (42.7%).

Keywords: light olefins; syngas; MgFe-LDH; MgO-FeO solid solution



Citation: Li, J.; Li, C.; Tang, Q.; Zuo, Z.; Liu, L.; Dong, J. Effect of MgFe-LDH with Reduction Pretreatment on the Catalytic Performance in Syngas to Light Olefins. *Catalysts* **2023**, *13*, 632. <https://doi.org/10.3390/catal13030632>

Academic Editor: Javier Ereña

Received: 13 February 2023

Revised: 17 March 2023

Accepted: 20 March 2023

Published: 21 March 2023



Copyright: © 2023 by the authors. Licensee MDPI, Basel, Switzerland. This article is an open access article distributed under the terms and conditions of the Creative Commons Attribution (CC BY) license (<https://creativecommons.org/licenses/by/4.0/>).

1. Introduction

As the main structural units and raw materials of many fine chemical products, light olefins (C₂–C₄) are traditionally mainly produced by the steam cracking and fluid catalytic cracking of naphtha [1,2]. With the increasing depletion of petroleum resources and the implementation of sustainable development strategies, it is more attractive to produce light olefins from syngas, which is extracted from non-petroleum carbon resources such as natural gas, coal and renewable biomass. The production of light olefins includes indirect routes such as methanol-to-olefins (MTO), dimethyl ether-to-olefins (DMTO), the dehydration of alcohols, and direct route FischerTropsch to olefins (FTO). Since the direct route is more economical than the indirect route after a long research period, the FTO route that directly converts syngas to lower olefins is expected to replace the traditional production route [3–6].

Since the FischerTropsch synthesis (FTS) process follows the Anderson–Schultz–Flory (ASF) distribution [7,8], resulting in wide production distribution, the selectivity of C₂–C₄ hydrocarbons is usually lower than 58% [6]. Therefore, the FTO reaction usually needs to be carried out at a high temperature (>200 °C) to obtain a higher selectivity to light olefins [6,8]. However, with the increase in reaction temperature, the side reaction Water Gas Shift (WGS), which is one of the primary generation pathways of CO₂ [9,10], will be

kinetically accelerated [11], resulting in over 40% of CO being converted to CO₂ in the majority of FTO catalysts [2,8,12–16]. In previous work, Bao et al. and Wang et al. proposed the concept of metal oxide and zeolite (OX-ZEO) catalysts that coupled CO activation and C-C coupling processes at different active sites [17,18]. High olefin selectivity (80%) was obtained over OX-ZEO catalysts at a reaction temperature of 400 °C, but with a low CO conversion (<20%) and a fairly high CO₂ selectivity (≈50%).

Among all the studied metals, such as Fe, Co and Ru [6], Fe-based catalysts attract more attention due to their lower price and higher reactivity of FTO and WGS reactions [19–21]. In addition, Fe-based catalysts are easier to use to generate more initial olefins in a wide range of reaction temperatures and H₂/CO ratios [22–25]. Since de Jong and colleagues discovered that supported iron-based catalysts have excellent selectivity (61%) for light olefins in FTO [8], research on iron-based catalysts has increased rapidly [13,14,26–28]. In the research of various promoters and supports, the addition of alkaline-earth metal Mg has been found to promote the catalyst activity and olefin selectivity and also inhibit the formation of CO₂ by suppressing the WGS reaction [29–32]. Niemelä and Krause reported that Mg-modified Co/SiO₂ catalysts could reduce CO₂ production owing to the change in the electronic structure of the active sites [29]. The effect of alkaline-earth metal on the catalytic performance of Fe-based catalysts was studied by Luo and Davis, and they found that Mg could suppress the water–gas shift reaction, thereby inhibiting the rate of CO₂ formation [30]. Li and colleagues reported a similar effect of Mg on precipitated Fe/Cu/K/SiO₂ catalysts [31]. Zong et al. designed Mg and K dual-decorated iron catalysts supported on reduced graphene oxide (rGO), where the modification of Mg could suppress the formation of magnetite during FTO that inhibited the water–gas shift reaction, leading to the reduce of CO₂ selectivity [32].

Layered Double Hydroxide (LDH) is a unique anionic compound that belongs to a class of two-dimensional materials. The general chemical formula of LDH is $[M^{2+}_{1-x}M^{3+}_x(OH)_2]^{x+}(A^{n-})_{x/n} \cdot mH_2O$, where M^{2+} represents a divalent cation such as Mg²⁺, Fe²⁺, Co²⁺, Ni²⁺, Zn²⁺, and M^{3+} represents a trivalent cation such as Fe³⁺, Co³⁺, Al³⁺, etc. [33–35]. The divalent and trivalent metal cations in LDH are highly dispersed in the laminate and arranged in an orderly manner [36]. Therefore, the calcination of LDH under air atmosphere or its reduction under heating conditions will lead to in situ topological transformations to form metal oxides or metal–metal oxide composites [37,38]. The preparation of highly dispersed supported catalysts by calcining or reducing LDH precursors provides a new method to obtain catalysts with specific morphologies and surface structures [39–41]. The interaction between the active phase and support is greatly enhanced, and the particle size and stability of the catalysts can also be well controlled [42]. Ma et al. [43] synthesized the SMSI-type TiO_{2-x} overlayers decorated Ni nanoparticle catalysts via calcination and then reduced the NiTi-LDH precursor, and obtained the CO conversion of ~19.8% with ~64.6% selectivity to C₂₊ paraffins in the FTS process at 220 °C under atmospheric pressure. Recently, Han and coworkers prepared FeMgAl catalysts with a controllable Mg/Al ratio by precipitation method, which inhibited CO₂ selectivity to 28% when the CO conversion was 20% and the light olefin selectivity was 56%. It was proved that MgO and Al₂O₃ play a key role in regulating the surface/bulk properties of iron species, revealing the effect of Mg/Al ratio on CO and H₂ adsorption/reactivity activities and proposing a balanced strategy to control carbon chain growth capacity (α), the ratio of olefins/paraffins (O/P) and primary/secondary CO₂ formation pathways [44].

In this contribution, we successfully prepared a series of Fe-x (x represents the reduction temperature) catalysts by reducing MgFe-LDH with hydrogen at different temperatures. The state of the iron phase in Fe-x catalysts was investigated in detail by changing the reduction temperatures, and the structures and properties of various catalysts were characterized by XRD, SEM, TEM, H₂-TPR, XPS, CO₂-TPD, and H₂-TPD technologies. The catalytic performance of such catalysts was evaluated on the FTO reaction, and the effect of reaction conditions on the catalytic results was also investigated, such as temperature, the ratio of H₂/CO, and space velocity.

2. Results and Discussion

2.1. Catalyst Characterization

2.1.1. Crystalline Structure

Figure 1a confirmed the successful synthesis of MgFe-LDH nanosheets. The H₂ reduction process of the MgFe-LDH nanosheet at different temperatures (from 300 to 600 °C) was tracked by X-ray diffraction (XRD) in Figure 1b. Fe-300 (reduction temperature was 300 °C) lost the characteristic diffraction peaks of the LDH precursor and showed the diffraction peaks of MgO (JCPDS No. 45-0496) at 42.9° (200) and 62.3° (220), and γ -Fe₂O₃ (JCPDS No. 04-0755) at 35.6° (311); this was mainly due to the removal of some interlayer anions and water molecules. When the reduction temperature rose to 400 °C (Fe-400), the crystal facets shifted to lower angles, located at 42.5° and 61.7°, respectively, between diffraction peaks of MgO and FeO, indicating that FeO (2.14 Å), gradually dissolved into the crystal lattice of MgO (2.10 Å), led to MgO-FeO (JCPDS No. 77-2366) solid solution being formed [45–47]. As the reduction temperature further increased to 500 °C (Fe-500), the (110) facet of Fe⁰ (JCPDS No. 87-0722) appeared at 44.7°. With the increase in reduction temperature, the diffraction peak intensities of MgO-FeO solid solution and Fe⁰ gradually increased. This showed that the reduction degree of the iron phase becomes higher, which is described in detail in the H₂-TPR characterization in Section 2.1.5.

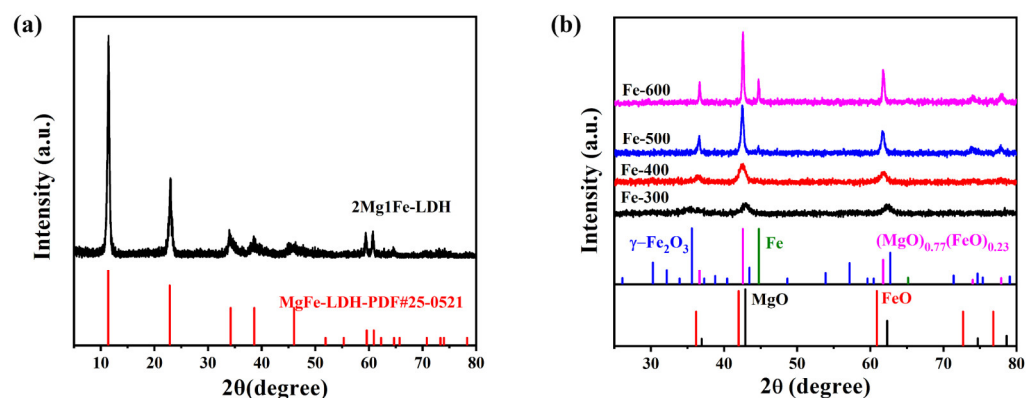


Figure 1. XRD patterns of the catalysts: (a) MgFe-LDH precursor; (b) Fe-x reduced at different temperatures.

2.1.2. Textural Properties

N₂ adsorption–desorption isotherms of the samples and the physical properties extracted from them were shown in Figure 2 and Table 1, respectively. All the catalysts showed type IV isotherms according to the IUPAC classification [48], all of them with mesoporous structures. When the relative pressure was low, the adsorption and desorption branches almost coincided due to the monolayer adsorption of N₂ on the mesoporous catalysts. Hysteresis loops occurred because the adsorption branch rose faster than the desorption branch at moderate relative pressures [49]. In addition to this, all the samples exhibited H3-type hysteresis loops, which we believed were caused by the accumulation of flake particles. As shown in Table 1, the specific surface area and pore volume of Fe-400 increased, possibly due to the further removal of interlaminar anions and bound water. When the reduction temperature was further increased (>500 °C), the specific surface area and pore volume suddenly decreased, which may be related to the aggregation of MgO-FeO species [50].

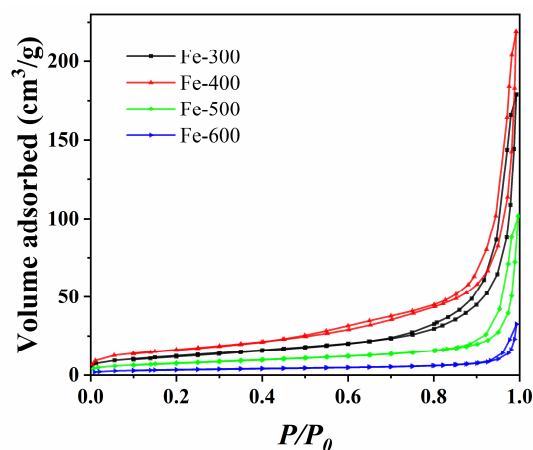


Figure 2. N₂ adsorption–desorption isotherms of the catalysts.

Table 1. The primary pore structure properties of the catalysts.

Samples	Surface Area (m ² ·g ^{−1})	Pore Volume (m ³ ·g ^{−1})	Pore Size (nm)
Fe-300	50.6	0.28	13.1
Fe-400	70.9	0.34	11.6
Fe-500	28.6	0.14	9.0
Fe-600	9.7	0.05	5.8

2.1.3. SEM Analysis

SEM images of MgFe-LDH and Fe-*x* catalysts are shown in Figure 3. MgFe-LDH precursors were made of typical flower-like nanosheets, and the reduced catalysts below 500 °C maintained the nanosheet structures. Due to the stacking and inter-embedding of the nanosheets, all of the samples showed irregular slits holy structures [51]. When the reduction temperature was below 500 °C, it can be seen that the catalysts still maintained the sheet structure of LDH. The sheet structures were destroyed in the Fe-600 catalyst, indicating that high temperatures led to pore structure reorganization, which was consistent with the trend observed in the specific surface areas [50].

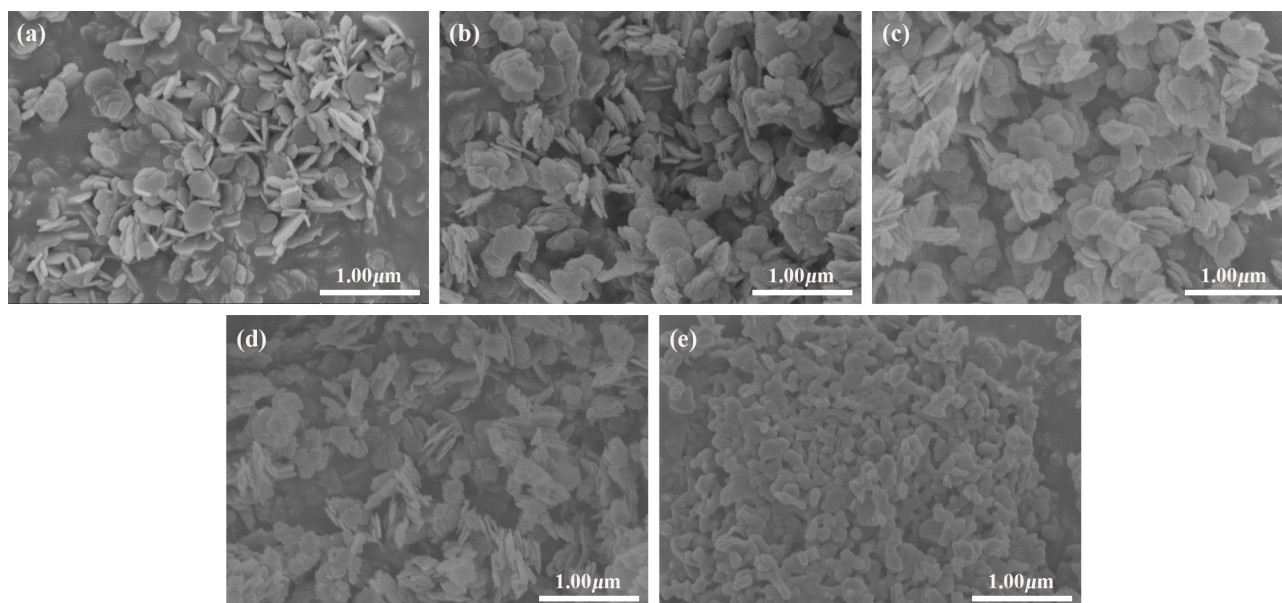


Figure 3. SEM images of the catalysts: (a) MgFe-LDH; (b) Fe-300; (c) Fe-400; (d) Fe-500; (e) Fe-600.

2.1.4. TEM Analysis

TEM images of the MgFe-LDH precursor and Fe-*x* catalysts are shown in Figure 4 and Figure S1. MgFe-LDH showed hexagonal lamellar structures of approximately 150 nm (Figure S1a). In the images of Fe-300, it can be seen that parts of the sheet structures fragmented into small particles, which were composed of MgO (200) and γ -Fe₂O₃ (311) (Figure 1b). Notably, a large number of pores appeared in the Fe-400 images (Figure S1b), which was mainly due to the layer collapse that occurred with the evolution of intercalated H₂O and small molecules during the conversion of LDH to metal oxides [52,53]. For Fe-500, only one lattice fringe with an average distance of 2.14 Å can be seen, which belonged to FeO-MgO (Figure 1d). Since the ionic radius and lattice constant of MgO and FeO are similar, they can form an ideal solid solution in all composition ranges [54,55]. When the reduction temperature was further increased to 600 °C, FeO diffused from the surface layer of the solid solution to the bulk phase (Figure S1c) [56].

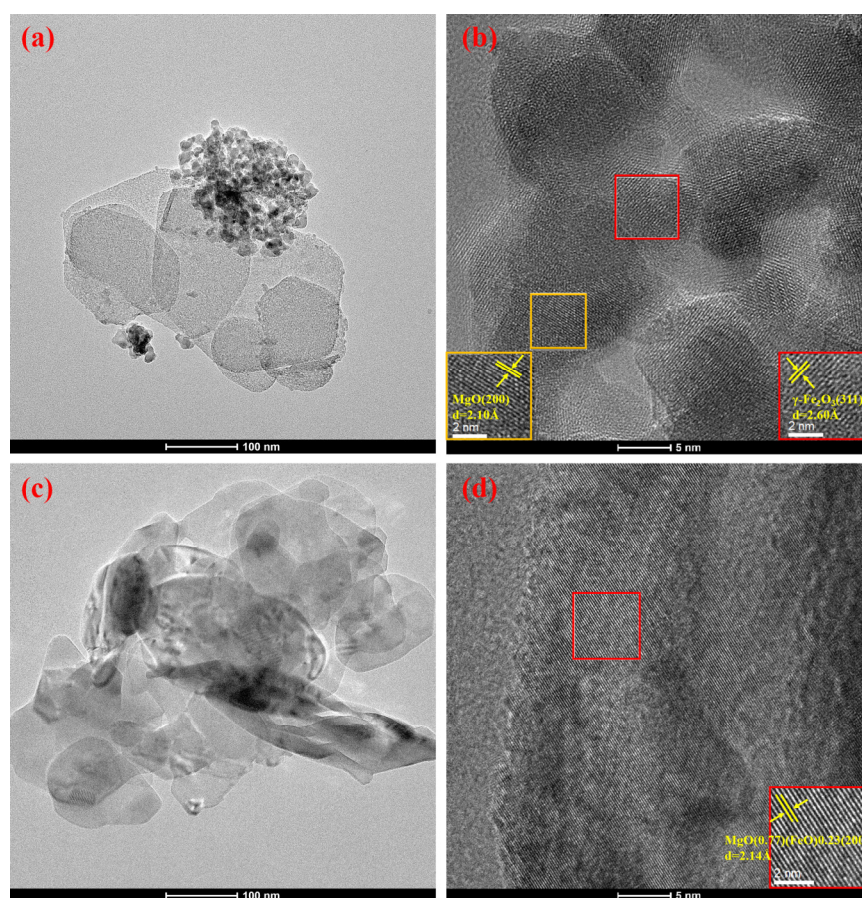


Figure 4. HRTEM images of the catalysts: (a,b) Fe-300; (c,d) Fe-500.

2.1.5. H₂-TPR Measurement of the Catalysts

The reduction behavior of the Fe-*x* series catalysts was tested by H₂ temperature-programmed reduction (TPR), and the results were shown in Figure 5. It can be seen that the reduction of the catalysts was mainly divided into two stages. The peak α between 250 and 500 °C represented the transition from Fe₂O₃ to Fe₃O₄, and included some Fe₃O₄ to FeO transitions. Due to the poor stability of FeO, when the reduction temperature was higher than 500 °C Fe₃O₄ and FeO were reduced to Fe⁰ at the same time, which was recorded as peak β [20,57]. The peak α and peak β shifted to lower temperature regions from sample Fe-300 to Fe-500. This may be due to the electrons gradually transferring from Mg to Fe during the process of structural transition, resulting in an easier reduction of FeO_{*x*}. This phenomenon would be demonstrated in the XPS characterization in Section 2.1.6.

However, for Fe-600 the reduction peaks shifted significantly to a high temperature. This may be due to the high temperature intensifying the diffusion of FeO from the surface layer of the sample to the bulk phase, increasing the depth of FeO entering the MgO particles, making it difficult to reduce [56]. In addition, the positions of the two reduction peaks, peak α and peak β of the catalysts, as well as the H₂ consumption, were listed in Table 2. As the reduction temperature increases, the H₂ consumption of peak α decreases significantly, indicating that a large amount of Fe₂O₃ was reduced to FeO, which coincided with the XRD characterization results.

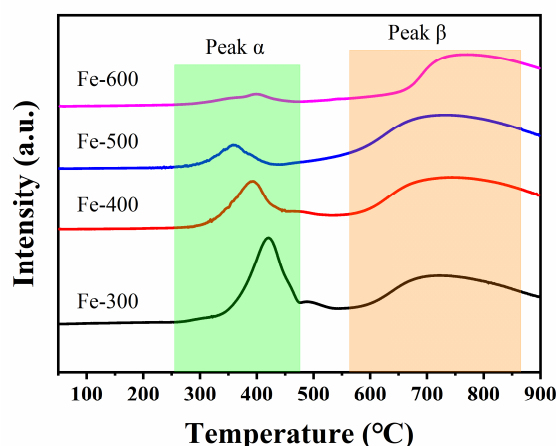


Figure 5. H₂-TPR profiles of the catalysts.

Table 2. Reduction peak temperature and H₂ consumption of the catalysts.

Samples	Peak α		Peak β	
	T/°C	n (H ₂)/(mmol/g)	T/°C	n (H ₂)/(mmol/g)
Fe-300	421	2.773	708	2.625
Fe-400	393	1.679	723	2.748
Fe-500	358	0.678	707	3.470
Fe-600	399	0.339	742	2.156

2.1.6. XPS Analysis of the Catalysts

The surface electronic structure of the catalysts was measured by XPS. As shown in Figure 6a, two peaks of the samples, at 710.8 eV and 724.4 eV, are attributed to Fe2p_{3/2} and Fe2p_{1/2} of the Fe₂O₃ phase, respectively [58–60]. Starting with Fe-400, there are two peaks attributed to FeO at 709.6 eV and 723.2 eV [60]. The peak value of FeO in Fe-500 became stronger. In addition, Fe-500 and Fe-600 also had two peaks attributed to Fe⁰ at 706.7 eV and 719.8 eV, and the peak value of Fe⁰ was stronger. Combined with the characterization results of XRD and H₂-TPR, the iron phase in Fe-300 was mainly Fe₂O₃, which gradually transformed to FeO and Fe⁰ with the increase in the reduction temperature. In Table 2, the peak β H₂ consumption (2.156 mmol/g) of Fe-600 is significantly lower than that of Fe-500 (3.470 mmol/g), indicating that when the reduction temperature was increased to 600 °C, the Fe⁰ phase increased significantly, so the consumption of H₂ during H₂-TPR process decreased. As can be seen in Figure 6b, the peaks that appeared at 49.7 eV belonged to MgO. As the reduction temperature increased, the binding energy of Mg atoms shifted toward higher positions; this was because electrons could transfer from Mg atoms to Fe atoms. Obviously, Fe-500 has the lowest Mg atomic valence, which is speculated to be due to the highest proportion of the MgO-FeO solid solution phase in Fe-500, and the existence of this phase is more conducive to the electron transfer from Mg atoms to Fe atoms.

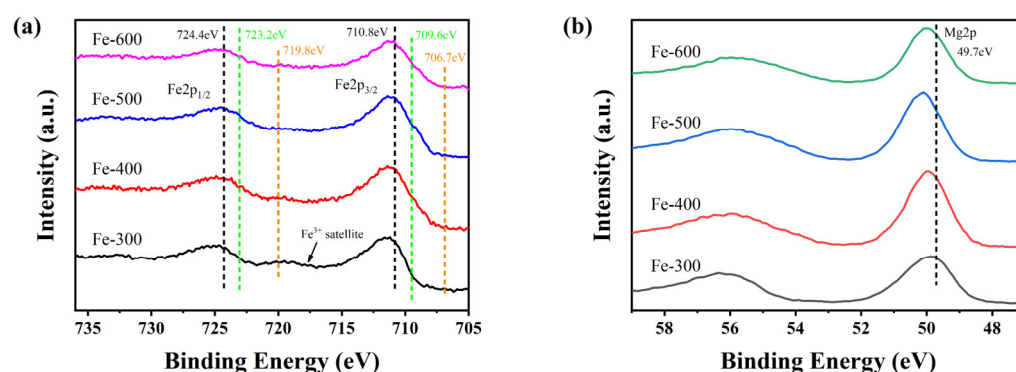


Figure 6. XPS spectra of the catalysts: (a) XPS spectra of Fe2p; (b) XPS spectra of Mg2p.

2.1.7. Chemisorption Properties of the Catalysts

The surface basicity of the catalysts was studied by CO₂ temperature-programmed desorption (CO₂-TPD), and the results were shown in Figure 7a. All of the samples had two desorption peaks at about 90 °C and 285 °C, the former corresponding to weakly physically adsorbed CO₂ and the latter to weakly chemisorbed CO₂ [60–62]. With the increase in the reduction temperature, the intensity of the desorption peak at 90 °C increased significantly, and reached the highest value at Fe-500, indicating that the CO₂ amount of weak physical adsorption increased, and the weak basicity of the catalyst surface increased. With the increase in the reduction temperature, the intensity of the desorption peak at 285 °C also increased slightly, indicating that the medium basicity of the catalyst surface was slightly enhanced and its degree was not as obvious as that of weak physical adsorption. When the reduction temperature is increased to 600 °C, the weak basicity of Fe-600 decreases significantly. The enhancement of the alkalinity of the catalyst surface is conducive to the adsorption and dissociation of CO, which leads to the increase of CO conversion and the length of the carbon chain, in addition to the ratio of olefins/paraffins.

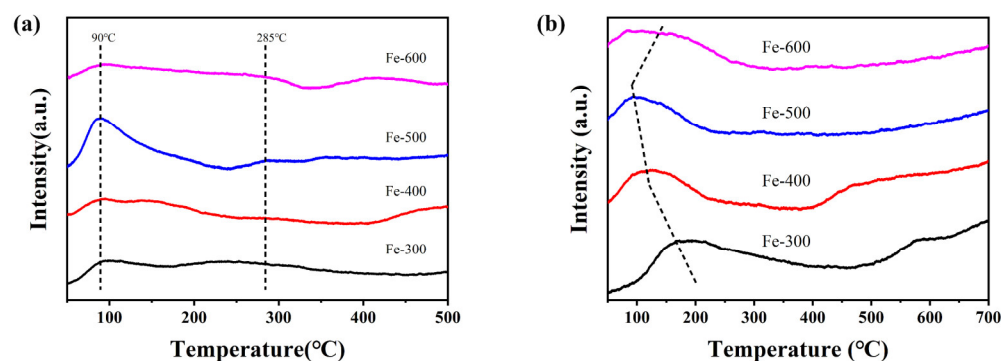


Figure 7. Chemisorption profiles of the catalysts: (a) CO₂-TPD profiles; (b) H₂-TPD profiles.

The adsorption capacity to hydrogen of the catalysts was studied by H₂ temperature-programmed desorption (H₂-TPD), and the results are shown in Figure 7b. According to previous studies, the desorption peak located at 100–300 °C represented the chemisorption of H₂ [60,63]. From Fe-300 to Fe-500, the desorption temperature gradually decreased, indicating that the adsorption capacity for H₂ became weaker with the increase of the reduction temperature. Fe-500 had the lowest H₂ desorption temperature, indicating that its adsorption and dissociation ability to H₂ was the weakest, which can inhibit the secondary hydrogenation reaction of olefins generated during FTO process well, thereby improving the selectivity of olefins. According to XPS, this may be due to the electrons transferred from Mg atoms to Fe atoms, resulting in higher electron density of the catalysts [60]. However, the desorption peak of Fe-600 shifted slightly to a high temperature, indicating that the adsorption capacity of H₂ was enhanced. This would promote the secondary

hydrogenation of the olefins, resulting in the increased selectivity of paraffins during the FTO process.

2.2. Catalytic Performance

2.2.1. The Activity and Selectivity of the Catalysts

The catalytic performances of the catalysts were shown in Table 3. The carbon balance of all the reactions was above 95%. From the sample Fe-300 to Fe-500, the CO conversion increased significantly from 8.11% to 29.94%. However, for Fe-600, the CO conversion suddenly dropped to 7.10%. Combined with the characterization results of XRD, H₂-TPR and XPS, due to the formation of MgO-FeO solid solution, the electrons transferred from Mg atoms to Fe atoms, resulting in the high electron density of Fe atoms, which was beneficial to the adsorption of CO, thereby generating FeC_x active sites in situ during the reaction process and ultimately improving CO conversion. At the same time, XPS, CO₂-TPD and H₂-TPD analysis proved that the strong basicity and strong electron density on the surface of the Fe-500 catalyst could inhibit the adsorption of H₂; that is, it could weaken the hydrogenation reaction, which would not only reduce the selectivity of CH₄ but also inhibit the secondary hydrogenation reaction of the olefins, thereby improving the ratio of olefins/paraffins (O/P) of the product [60,64]. For Fe-600, due to the stacking of lamellae when the temperature was above 600 °C, many active sites were covered, resulting in a significant decrease in CO conversion.

Table 3. Catalytic performance of the catalysts.

Samples	CO Conversion (%)	CO ₂ Selectivity (%)	Hydrocarbon Distribution (%)				O/P (C ₂ –C ₄)
			CH ₄	C ₂ –C ₄ [≡]	C ₂ –C ₄ ⁰	C ₅ ⁺	
Fe-300	8.11	13.27	30.47	35.97	22.22	11.34	1.62
Fe-400	9.20	3.93	27.49	44.74	21.45	6.32	2.09
Fe-500	29.94	19.43	24.11	42.68	14.96	18.25	2.85
Fe-600	7.10	5.87	31.06	42.11	18.98	7.85	2.22

Reaction conditions: H₂/CO = 2.0, GHSV = 2000 h^{−1}, T = 300 °C, P = 2.0 MPa.

2.2.2. The Effects of the Reaction Conditions over the Fe-500 Catalyst

As we all know, reaction temperature is one of the important factors affecting the selectivity of the light olefins, so we evaluated the CO hydrogenation performance of the Fe-500 catalyst at different reaction temperatures, and the results are listed in Figure 8a. With the increase in reaction temperature, the CO conversion increased sharply and the selectivity of CO₂ also increased significantly. For the distribution of hydrocarbon products, the increase of reaction temperature led to the movement of products in the direction of low carbon, the selectivity of CH₄ increased, and the selectivity of C₅⁺ decreased. In addition, a larger proportion of alkanes was observed, which was due to the increase in temperature, leading to the secondary hydrogenation of alkenes on the surface of the catalyst to form alkanes [65]. In contrast, we chose the reaction temperature of 330 °C for the next study.

As shown in Figure 8b, the effect of the H₂/CO ratio of feed gas on catalytic performance has also been studied. With the increase of the H₂/CO ratio, the CO conversion rate first increased and then decreased, and the CO₂ selectivity showed a similar trend. When the H₂/CO ratio was 2:1, CO conversion and CO₂ selectivity reached the highest point: 78% and 43%, respectively. In this process, CH₄ selectivity slightly increased and C₅⁺ selectivity slightly decreased. The value of O/P changes obviously, which is the opposite trend to the change of CO conversion. With the increase of the H₂/CO ratio, the content of C₂–C₄ olefins decreases first and then increases. To sum up, we chose the H₂/CO ratio of 1.5:1 for the next study.

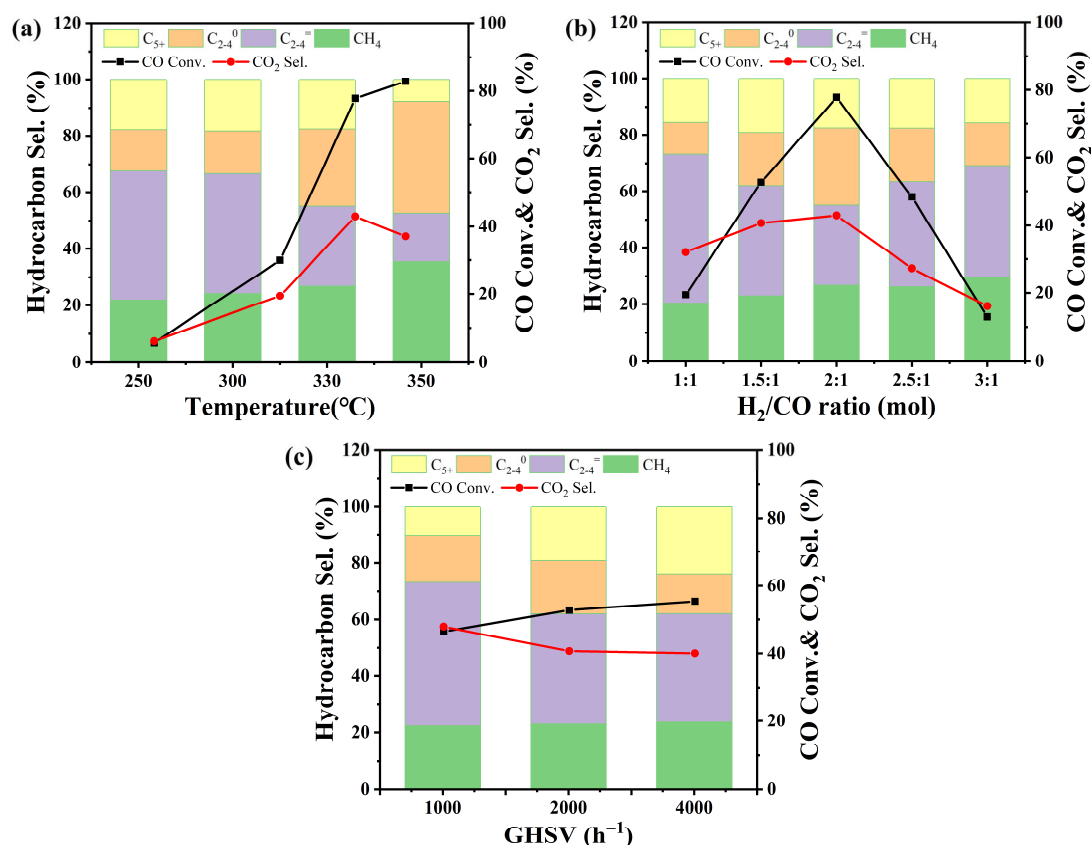


Figure 8. The effects of the reaction conditions for the Fe-500 catalyst: (a) reaction temperature; (b) H₂/CO ratio; (c) space velocity.

In addition, we also studied the effect of reaction space velocity on catalytic performance, as shown in Figure 8c. With the increase of reaction space velocity, CO conversion increased slightly and CO₂ selectivity decreased. For hydrocarbons in the product, CH₄ selectivity was almost unchanged ($\approx 20\%$) and C₅₊ selectivity was significantly increased from 10% to 24%. The proportion of C₂–C₄ hydrocarbons decreased from 68% to 53%, with O/P slightly decreased. When GHSV was 1000 h⁻¹, C₂–C₄ olefins selectivity was 51%, with O/P 3.10. In summary, the optimal reaction conditions of the Fe-500 catalyst were 330 °C, H₂/CO = 1.5:1, GHSV = 1000 h⁻¹. We compared the data with previous works, which were listed in Table S1.

3. Materials and Methods

3.1. Catalyst Preparation

3.1.1. Synthesis of the MgFe-CO₃-LDH Precursor

MgFe-CO₃-LDH was prepared by the hydrothermal method. In brief, 2.7602 g Na₂CO₃ was dissolved into 60.7 mL of distilled water, named solution A. Then, 10.4 mL of Mg(NO₃)₂ aqueous solution (2 mol/L) was added into solution A under vigorous stirring. Similarly, 5.2 mL of Fe(NO₃)₃ (2 mol/L) aqueous solution was added to the above solution. Finally, 3.9 mL of NaOH solution (9.67 mol/L) was added to adjust the pH value, with constant stirring. The obtained mixed solution was transferred into a 100 mL Teflon-lined autoclave, and then moved into the laboratory oven for further heating at 100 °C for 3 days. The obtained red-brown solid was then filtered, washed with deionized water, and dried at 100 °C for 12 h. Thus, the precursor MgFe-CO₃-LDH was obtained.

3.1.2. Synthesis of Fe-X Catalysts

MgFe-CO₃-LDH was reduced in an H₂/Ar (10/90, *v/v*) flow at different reduction temperatures (300, 400, 500, 600 °C) for 180 min with a heating rate of 2 °C/min. The products were named Fe-x, where x refers to the reduction temperature.

3.2. Catalyst Characterization

Powder X-ray diffraction (XRD) patterns of all samples were determined using a Rigaku Ultima IV (Rigaku Corporation, Tokyo, Japan) powder diffractometer and tested with Cu K α radiation at 40 kV and 40 mA.

The textural properties of the samples were obtained by recording the N₂ adsorption-desorption isotherms at −196 °C on the Micromeritics ASAP 2020 PLUS HD88 (Micromeritics, Norcross, GA, USA), and the samples were pretreated at 110 °C for 10 h before testing. The specific surface area and pore size distribution of the samples were calculated by Brunauer-Emmett-Teller and Barrett-Joyner-Halenda methods, respectively.

Scanning electron microscopy (SEM) images were obtained with a JSM-7001F (Japan Electronics Co., Ltd., Tokyo, Japan) instrument with a voltage of 3.0 kV and 30,000 times amplification.

High-resolution transmission electron microscopy (HRTEM) images of the samples were acquired on a JEOL JEM 2100F (Japan Electronics Co., Ltd., Tokyo, Japan) with an acceleration voltage of 200 kV.

The H₂ temperature-programmed reduction (H₂-TPR) curves of the samples were used to record the reducibility of the catalysts on Micromeritics AutoChem II 2920 (Micromeritics, Norcross, GA, USA). A total of 50 mg of catalyst was put into a quartz tube, pretreated with He at 110 °C for 1 h, then cooled to 50 °C for 30 min. Additionally, it was then switched to a 4.85% H₂/Ar mixture; after the baseline was stable, the temperature was increased to 900 °C by the rate of 10 °C/min and H₂ consumption was recorded.

The chemical state of the elements on the surface of the catalysts was detected by X-ray photoelectron spectroscopy and tested on ThermoFischer ESCALAB 250Xi (Thermo Fischer Scientific, Waltham, MA, USA) equipped with a monochromatized Al K α radiation source. The operating voltage was 12.5 kV, and the current was 16 mA. Data calibration was performed using the peak C1s of 284.6 eV.

CO₂ temperature-programmed desorption (CO₂-TPD) curves were recorded on the TPR-tested equipment. A total of 50 mg of the catalyst was pretreated at 500 °C for 1 h, and then cooled to 50 °C. The samples were exposed to a flow of CO₂ for 40 min and then switched to a flow of He purged for 40 min to remove physically adsorbed CO₂ species. Finally, the temperature was raised to 500 °C at a heating rate of 10 °C/min, and the desorption signal of CO₂ was recorded by a thermal conductivity detector (TCD).

H₂ temperature-programmed desorption (H₂-TPD) curves were recorded on the TPD-tested equipment. A total of 50 mg of the catalyst was pretreated at 500 °C for 1 h and then cooled to 50 °C. The samples were exposed to a flow of H₂ for 40 min and then switched to a flow of He purged for 40 min to remove physically adsorbed H₂ species. Finally, the temperature was raised to 500 °C at a heating rate of 10 °C/min, and the desorption signal of H₂ was recorded by a thermal conductivity detector (TCD).

3.3. Catalytic Activity Tests

CO hydrogenation reactions were performed in a stainless fixed-bed reactor loading 1 mL of catalyst (40–60 mesh). The feed gas (H₂/CO = 2, molar ratio) was introduced into the reactor with a pressure of 2 MPa and GHSV of 2000 h^{−1}. Nitrogen with a concentration of 10% in the syngas was used as an internal standard for the calculation of CO conversion. The reaction temperature was then ramped slowly to 300 °C. The permanent gases (H₂, N₂, CO, CH₄), light hydrocarbon (CH₄, C₂–C₄), and those gases (CO, CH, CO₂) that can be converted into methane were monitored by an online HXSP GC-950 (Haixinsepu Instrument Co., Ltd, Shanghai, China) gas chromatograph (GC) equipped with the 5A molecular sieve, modified Al₂O₃, and TDX-01 columns. The oil and wax products were

separated by a cold trap (0 °C) and a hot trap (150 °C). The oil products were analyzed using an Agilent 7890B (Agilent Technologies Co., Ltd, Santa Clara, CA, USA) GC with a DB-1 column. The product selectivity was calculated based on the carbon balance, and the carbon balance of each test in this work was above 95%.

CO conversion (X_{CO}) and product selectivity are calculated as follows:

$$X_{CO} = \left(1 - \frac{\frac{S_{N_2,in}}{S_{N_2,out}}}{\frac{S_{CO,in}}{S_{CO,out}}} \right) \times 100\% \quad (1)$$

$S_{N_2,in}$: the peak area of N_2 in the inflow; $S_{N_2,out}$: the peak area of N_2 in the outflow; $S_{CO,in}$: the peak area of CO in the inflow; $S_{CO,out}$: the peak area of CO in the outflow.

$$Selectivity_{CO_2} = \frac{n_{CO_2}}{n_{CO_2} + \sum n_{C_i}} \times 100\% \quad (2)$$

n_{CO_2} : carbon number of CO_2 in the products; n_{C_i} : carbon number of corresponding products.

$$Selectivity_{C_i} = \frac{n_{C_i}}{\sum n_{C_i}} \times 100\% \quad (3)$$

$$\frac{O}{P} = \frac{n_{C_{2-4}}^o}{n_{C_{2-4}}^p} \quad (4)$$

$n_{C_{2-4}}^o$: carbon number of C_{2-4} olefins in the products; $n_{C_{2-4}}^p$: carbon number of C_{2-4} paraffins in the products.

4. Conclusions

In conclusion, a series of Fe-x catalysts were prepared by reducing the MgFe-LDH precursor at different temperatures (300–600 °C). The Fe-500 catalyst acquired a CO conversion rate of 30%, light olefins selectivity of 43%, and a low CO_2 selectivity (19%) under the reaction conditions of 300 °C, $H_2/CO = 2:1$, GHSV = 2000 h^{-1} , 2 MPa. After a series of characterizations, it was proved that, with the increase in reduction temperature, the catalyst gradually evolved into FeO-MgO solid solution and Fe^0 . The formation of the MgO-FeO solid solution is conducive to the electrons transfer from Mg atoms to Fe atoms, so it enhanced the adsorption of CO to generate FeC_x active sites in situ during the reaction process, thereby improving CO conversion. In addition, the increase of the basicity and electron density on the surface of the catalysts weakened the adsorption of H_2 , inhibited the secondary hydrogenation reaction of the olefins while inhibiting the formation of methane, and improved the selectivity of light olefins and the O/P value of the product. We optimized the reaction conditions of the Fe-500 catalyst, and finally determined that the suitable reaction conditions were 330 °C, $H_2/CO = 1.5:1$, and GHSV = 1000 h^{-1} . Under these conditions, the CO conversion was 47%, the selectivity of light olefins was 51%, and the O/P value was 3.10. This study provides new routes for the preparation of novel FTO catalysts.

Supplementary Materials: The following supporting information can be downloaded at: <https://www.mdpi.com/article/10.3390/catal13030632/s1>, Figure S1: HRTEM images of the catalysts: (a) MgFe-LDH, (b) Fe-400, (c) Fe-600; Figure S2: XRD patterns of the spent catalysts; Table S1: Comparison of the catalytic performance with the previous works [8,12–14,17,18,26–28,66,67].

Author Contributions: Conceptualization, L.L. and J.D.; methodology, J.D., L.L. and J.L.; investigation, J.L. and C.L.; writing—original draft preparation, J.L.; writing—review and editing, L.L., Z.Z., Q.T. and J.L.; supervision, J.D.; project administration, J.D. and L.L.; funding acquisition, L.L. All authors have read and agreed to the published version of the manuscript.

Funding: This work was supported by the National Natural Science Foundation (U1910202 and 21978194), the Key Research and Development Program of Shanxi Province (202102090301005) and the Fund for Shanxi “1331 Project”.

Data Availability Statement: Not applicable.

Conflicts of Interest: The authors declare no conflict of interest.

References

1. Corma, A.; Melo, F.; Sauvanaud, L.; Ortega, F. Light cracked naphtha processing: Controlling chemistry for maximum propylene production. *Catal. Today* **2005**, *107*, 699–706. [\[CrossRef\]](#)
2. Torres Galvis, H.M.; Bitter, J.H.; Davidian, T.; Ruitenbeek, M.; Dugulan, A.I.; de Jong, K.P. Iron Particle Size Effects for Direct Production of Lower Olefins from Synthesis Gas. *J. Am. Chem. Soc.* **2012**, *134*, 16207–16215. [\[CrossRef\]](#) [\[PubMed\]](#)
3. Snel, R. Olefins from Syngas. *Catal. Rev. Sci. Eng.* **1987**, *29*, 361–445. [\[CrossRef\]](#)
4. Yang, Z.; Pan, X.; Wang, J.; Bao, X. FeN particles confined inside CNT for light olefin synthesis from syngas: Effects of Mn and K additives. *Catal. Today* **2012**, *186*, 121–127. [\[CrossRef\]](#)
5. Chen, X.; Deng, D.; Pan, X.; Hu, Y.; Bao, X. N-doped graphene as an electron donor of iron catalysts for CO hydrogenation to light olefins. *Chem. Commun.* **2014**, *51*, 217–220. [\[CrossRef\]](#)
6. Torres Galvis, H.M.; de Jong, K.P. Catalysts for Production of Lower Olefins from Synthesis Gas: A Review. *ACS Catal.* **2013**, *3*, 2130–2149. [\[CrossRef\]](#)
7. Puskas, I.; Hurlbut, R.S. Comments about the causes of deviations from the Anderson–Schulz–Flory distribution of the Fischer–Tropsch reaction products. *Catal. Today* **2003**, *84*, 99–109. [\[CrossRef\]](#)
8. Galvis, H.M.T.; Bitter, J.H.; Khare, C.B.; Ruitenbeek, M.; Dugulan, A.I.; de Jong, K.P. Supported Iron Nanoparticles as Catalysts for Sustainable Production of Lower Olefins. *Science* **2012**, *335*, 835–838. [\[CrossRef\]](#)
9. Krishnamoorthy, S.; Li, A.; Iglesia, E. Pathways for CO₂ Formation and Conversion During Fischer–Tropsch Synthesis on Iron-Based Catalysts. *Catal. Lett.* **2002**, *80*, 77–86. [\[CrossRef\]](#)
10. Botes, F.G. Water–gas-shift kinetics in the iron-based low-temperature Fischer–Tropsch synthesis. *Appl. Catal. A Gen.* **2007**, *328*, 237–242. [\[CrossRef\]](#)
11. Pirola, C.; Bianchi, C.L.; Di Michele, A.; Vitali, S.; Ragaini, V. Fischer Tropsch and Water Gas Shift chemical regimes on supported iron-based catalysts at high metal loading. *Catal. Commun.* **2009**, *10*, 823–827. [\[CrossRef\]](#)
12. Zhong, L.; Yu, F.; An, Y.; Zhao, Y.; Sun, Y.; Li, Z.; Lin, T.; Lin, Y.; Qi, X.; Dai, Y.; et al. Cobalt carbide nanoprisms for direct production of lower olefins from syngas. *Nature* **2016**, *538*, 84–87. [\[CrossRef\]](#)
13. Wang, J.; Xu, Y.; Ma, G.; Lin, J.; Wang, H.; Zhang, C.; Ding, M. Directly converting syngas to linear α -olefins over core-shell Fe₃O₄@MnO₂ catalysts. *ACS Appl. Mater. Interfaces* **2018**, *10*, 43578–43587. [\[CrossRef\]](#)
14. Santos, V.P.; Wezendonk, T.A.; Jaén, J.J.D.; Dugulan, A.I.; Nasalevich, M.A.; Islam, H.-U.; Chojecki, A.; Sartipi, S.; Sun, X.; Hakeem, A.A.; et al. Metal organic framework-mediated synthesis of highly active and stable Fischer–Tropsch catalysts. *Nat. Commun.* **2015**, *6*, 6451. [\[CrossRef\]](#)
15. Wang, C.; Pan, X.; Bao, X. Direct production of light olefins from syngas over a carbon nanotube confined iron catalyst. *Chin. Sci. Bull.* **2010**, *55*, 1117–1119. [\[CrossRef\]](#)
16. Chen, X.; Deng, D.; Pan, X.; Bao, X. Iron catalyst encapsulated in carbon nanotubes for CO hydrogenation to light olefins. *Chin. J. Catal.* **2015**, *36*, 1631–1637. [\[CrossRef\]](#)
17. Jiao, F.; Li, J.; Pan, X.; Xiao, J.; Li, H.; Ma, H.; Wei, M.; Pan, Y.; Zhou, Z.; Li, M.; et al. Selective conversion of syngas to light olefins. *Science* **2016**, *351*, 1065–1068. [\[CrossRef\]](#)
18. Cheng, K.; Gu, B.; Liu, X.; Kang, J.; Zhang, Q.; Wang, Y. Direct and Highly Selective Conversion of Synthesis Gas into Lower Olefins: Design of a Bifunctional Catalyst Combining Methanol Synthesis and Carbon–Carbon Coupling. *Angew. Chem.* **2016**, *128*, 4803–4806. [\[CrossRef\]](#)
19. Zhang, Y.; Ma, L.; Wang, T.; Li, X. MnO₂ coated Fe₂O₃ spindles designed for production of C₅+ hydrocarbons in Fischer–Tropsch synthesis. *Fuel* **2016**, *177*, 197–205. [\[CrossRef\]](#)
20. Li, Z.; Liu, R.; Xu, Y.; Ma, X. Enhanced Fischer–Tropsch synthesis performance of iron-based catalysts supported on nitric acid treated N-doped CNTs. *Appl. Surf. Sci.* **2015**, *347*, 643–650. [\[CrossRef\]](#)
21. Visconti, C.G.; Martinelli, M.; Falbo, L.; Infantes-Molina, A.; Lietti, L.; Forzatti, P.; Iaquaniello, G.; Palo, E.; Picutti, B.; Brignoli, F. CO₂ hydrogenation to lower olefins on a high surface area K-promoted bulk Fe-catalyst. *Appl. Catal. B Environ.* **2017**, *200*, 530–542. [\[CrossRef\]](#)
22. Li, S.; Krishnamoorthy, S.; Li, A.; Meitzner, G.D.; Iglesia, E. Promoted Iron-Based Catalysts for the Fischer–Tropsch Synthesis: Design, Synthesis, Site Densities, and Catalytic Properties. *J. Catal.* **2002**, *206*, 202–217. [\[CrossRef\]](#)
23. Dictor, R.A.; Bell, A.T. Fischer–Tropsch synthesis over reduced and unreduced iron oxide catalysts. *J. Catal.* **1986**, *97*, 121–136. [\[CrossRef\]](#)
24. Yang, Y.; Xiang, H.W.; Xu, Y.Y.; Bai, L.; Li, Y.W. Effect of potassium promoter on precipitated iron-manganese catalyst for Fischer–Tropsch synthesis. *Appl. Catal. A Gen.* **2004**, *266*, 181–194. [\[CrossRef\]](#)

25. Zhang, J.-L.; Ma, L.-H.; Fan, S.-B.; Zhao, T.-S.; Sun, Y.-H. Synthesis of light olefins from CO hydrogenation over Fe–Mn catalysts: Effect of carburization pretreatment. *Fuel* **2013**, *109*, 116–123. [\[CrossRef\]](#)
26. Lu, J.; Yang, L.; Xu, B.; Wu, Q.; Zhang, D.; Yuan, S.; Zhai, Y.; Wang, X.; Fan, Y.; Hu, Z. Promotion Effects of Nitrogen Doping into Carbon Nanotubes on Supported Iron Fischer–Tropsch Catalysts for Lower Olefins. *ACS Catal.* **2014**, *4*, 613–621. [\[CrossRef\]](#)
27. Liu, Y.; Chen, J.-F.; Bao, J.; Zhang, Y. Manganese-Modified Fe₃O₄ Microsphere Catalyst with Effective Active Phase of Forming Light Olefins from Syngas. *ACS Catal.* **2015**, *5*, 3905–3909. [\[CrossRef\]](#)
28. Zhuo, O.; Yang, L.; Gao, F.; Xu, B.; Wu, Q.; Fan, Y.; Zhang, Y.; Jiang, Y.; Huang, R.; Wang, X.; et al. Stabilizing the active phase of iron-based Fischer–Tropsch catalysts for lower olefins: Mechanism and strategy. *Chem. Sci.* **2019**, *10*, 6083–6090. [\[CrossRef\]](#)
29. Niemelä, M.K.; Krause, A.O.I. Characterization of magnesium promoted Co/SiO₂ catalysts. *Catal. Lett.* **1995**, *34*, 75–84. [\[CrossRef\]](#)
30. Luo, M.; Davis, B.H. Fischer–Tropsch synthesis: Group II alkali-earth metal promoted catalysts. *Appl. Catal. A Gen.* **2003**, *246*, 171–181. [\[CrossRef\]](#)
31. Yang, J.; Sun, Y.; Tang, Y.; Liu, Y.; Wang, H.; Tian, L.; Wang, H.; Zhang, Z.; Xiang, H.; Li, Y. Effect of magnesium promoter on iron-based catalyst for Fischer–Tropsch synthesis. *J. Mol. Catal. A Chem.* **2006**, *245*, 26–36. [\[CrossRef\]](#)
32. Cheng, Y.; Lin, J.; Wu, T.; Wang, H.; Xie, S.; Pei, Y.; Yan, S.; Qiao, M.; Zong, B. Mg and K dual-decorated Fe-on-reduced graphene oxide for selective catalyzing CO hydrogenation to light olefins with mitigated CO₂ emission and enhanced activity. *Appl. Catal. B Environ.* **2017**, *204*, 475–485. [\[CrossRef\]](#)
33. Cavani, F.; Trifirò, F.; Vaccari, A. Hydrotalcite-type anionic clays: Preparation, properties and applications. *Catal. Today* **1991**, *11*, 173–301. [\[CrossRef\]](#)
34. Brindley, G.W.; Kikkawa, S. Thermal Behavior of Hydrotalcite and of Anion-Exchanged Forms of Hydrotalcite. *Clays Clay Miner.* **1980**, *28*, 87–91. [\[CrossRef\]](#)
35. Wang, Q.; O'Hare, D. Recent Advances in the Synthesis and Application of Layered Double Hydroxide (LDH) Nanosheets. *Chem. Rev.* **2012**, *112*, 4124–4155. [\[CrossRef\]](#)
36. Sideris, P.J.; Nielsen, U.G.; Gan, Z.; Grey, C.P. Mg/Al Ordering in Layered Double Hydroxides Revealed by Multinuclear NMR Spectroscopy. *Science* **2008**, *321*, 113–117. [\[CrossRef\]](#)
37. Li, C.; Wang, L.; Wei, M.; Evans, D.G.; Duan, X. Large oriented mesoporous self-supporting Ni–Al oxide films derived from layered double hydroxide precursors. *J. Mater. Chem.* **2008**, *18*, 2666–2672. [\[CrossRef\]](#)
38. He, S.; Zhang, S.; Lu, J.; Zhao, Y.; Ma, J.; Wei, M.; Evans, D.G.; Duan, X. Enhancement of visible light photocatalysis by grafting ZnO nanoplatelets with exposed (0001) facets onto a hierarchical substrate. *Chem. Commun.* **2011**, *47*, 10797–10799. [\[CrossRef\]](#)
39. He, S.; Li, C.; Chen, H.; Su, D.; Zhang, B.; Cao, X.; Wang, B.; Wei, M.; Evans, D.G.; Duan, X. A Surface Defect-Promoted Ni Nanocatalyst with Simultaneously Enhanced Activity and Stability. *Chem. Mater.* **2013**, *25*, 1040–1046. [\[CrossRef\]](#)
40. Zhao, Y.; Li, Z.; Li, M.; Liu, J.; Liu, X.; Waterhouse, G.I.N.; Wang, Y.; Zhao, J.; Gao, W.; Zhang, Z.; et al. Reductive Transformation of Layered-Double-Hydroxide Nanosheets to Fe-Based Heterostructures for Efficient Visible-Light Photocatalytic Hydrogenation of CO. *Adv. Mater.* **2018**, *30*, 1803127. [\[CrossRef\]](#)
41. Li, Z.; Liu, J.; Shi, R.; Waterhouse, G.I.; Wen, X.D.; Zhang, T. FeBased Catalysts for the Direct Photohydrogenation of CO₂ to Value-Added Hydrocarbons. *Adv. Energy Mater.* **2021**, *11*, 2002783. [\[CrossRef\]](#)
42. Fan, G.; Li, F.; Evans, D.G.; Duan, X. Catalytic applications of layered double hydroxides: Recent advances and perspectives. *Chem. Soc. Rev.* **2014**, *43*, 7040–7066. [\[CrossRef\]](#) [\[PubMed\]](#)
43. Xu, M.; Qin, X.; Xu, Y.; Zhang, X.; Zheng, L.; Liu, J.-X.; Wang, M.; Liu, X.; Ma, D. Boosting CO hydrogenation towards C₂₊ hydrocarbons over interfacial TiO_{2-x}/Ni catalysts. *Nat. Commun.* **2022**, *13*, 6720. [\[CrossRef\]](#) [\[PubMed\]](#)
44. Liu, Y.; Xu, M.; Yang, Z.; Ding, X.; Zhu, M.; Han, Y.F. Syngas to olefins with low CO₂ formation by tuning the structure of Fe₂Cx-MgO-Al₂O₃ catalysts. *Chem. Eng. J.* **2022**, *450*, 137167. [\[CrossRef\]](#)
45. Hu, Y.H.; Ruckenstein, E. High-Resolution Transmission Electron Microscopy Study of Carbon Deposited on the NiO/MgO Solid Solution Catalysts. *J. Catal.* **1999**, *184*, 298–302. [\[CrossRef\]](#)
46. Lu, Y.; Jiang, S.; Wang, S.; Zhao, Y.; Ma, X. Effect of the addition of Ce and Zr over a flower-like NiO–MgO (111) solid solution for CO₂ reforming of methane. *J. CO₂ Util.* **2018**, *26*, 123–132. [\[CrossRef\]](#)
47. Chen, Z.; Liu, J.; Li, R. Simulation and property prediction of MgO–FeO–MnO solid solution in steel slag. *Mater. Lett.* **2020**, *273*, 127930. [\[CrossRef\]](#)
48. Liu, H.; Xu, S.; Zhou, G.; Xiong, K.; Jiao, Z.; Wang, S. CO₂ hydrogenation to methane over Co/KIT-6 catalysts: Effect of Co content. *Fuel* **2018**, *217*, 570–576. [\[CrossRef\]](#)
49. Zhou, G.; Liu, H.; Cui, K.; Xie, H.; Jiao, Z.; Zhang, G.; Xiong, K.; Zheng, X. Methanation of carbon dioxide over Ni/CeO₂ catalysts: Effects of support CeO₂ structure. *Int. J. Hydrogen Energy* **2017**, *42*, 16108–16117. [\[CrossRef\]](#)
50. Liu, Z.; Gao, X.; Liu, B.; Song, W.; Ma, Q.; Zhao, T.-S.; Wang, X.; Bae, J.W.; Zhang, X.; Zhang, J. Highly stable and selective layered Co–Al–O catalysts for low-temperature CO₂ methanation. *Appl. Catal. B Environ.* **2022**, *310*, 121303. [\[CrossRef\]](#)
51. Zhang, F.; Lu, B.; Sun, P. Co-Promoted Ni Nanocatalysts Derived from NiCoAl-LDHs for Low Temperature CO₂ Methanation. *Catalysts* **2021**, *11*, 121. [\[CrossRef\]](#)
52. Kobayashi, Y.; Ke, X.; Hata, H.; Schiffer, P.; Mallouk, T.E. Soft Chemical Conversion of Layered Double Hydroxides to Superparamagnetic Spinel Platelets. *Chem. Mater.* **2008**, *20*, 2374–2381. [\[CrossRef\]](#)
53. Xu, Y.; Wang, Z.; Tan, L.; Zhao, Y.; Duan, H.; Song, Y.-F. Fine Tuning the Heterostructured Interfaces by Topological Transformation of Layered Double Hydroxide Nanosheets. *Ind. Eng. Chem. Res.* **2018**, *57*, 10411–10420. [\[CrossRef\]](#)

54. Yoshida, T.; Tanaka, T.; Yoshida, H.; Funabiki, T.; Yoshida, S. Study on the dispersion of nickel ions in the NiO–MgO system by X-ray absorption fine structure. *J. Phys. Chem. C* **1996**, *100*, 2302–2309. [[CrossRef](#)]
55. Arena, F.; Frusteri, F.; Parmaliana, A.; Plyasova, L.; Shmakov, A.N. Effect of calcination on the structure of Ni/MgO catalyst: An X-ray diffraction study. *J. Chem. Soc. Faraday Trans.* **1996**, *92*, 469–471. [[CrossRef](#)]
56. Wang, Y.; Liu, H.; Xu, B. Effect of Formation of NiO–MgO Solid Solution on Activity and Stability of Ni/MgO–AN for CO₂ Reforming of Methane. *Chin. J. Catal.* **2005**, *26*, 1117.
57. Qing, M.; Yang, Y.; Wu, B.; Xu, J.; Zhang, C.; Gao, P.; Li, Y. Modification of Fe–SiO₂ interaction with zirconia for iron-based Fischer–Tropsch catalysts. *J. Catal.* **2011**, *279*, 111–122. [[CrossRef](#)]
58. Jia, C.-J.; Sun, L.-D.; Luo, F.; Han, X.-D.; Heyderman, L.J.; Yan, Z.-G.; Yan, C.-H.; Zheng, K.; Zhang, Z.; Takano, M.; et al. Large-Scale Synthesis of Single-Crystalline Iron Oxide Magnetic Nanorings. *J. Am. Chem. Soc.* **2008**, *130*, 16968–16977. [[CrossRef](#)]
59. Han, Z.; Qian, W.; Ma, H.; Wu, X.; Zhang, H.; Sun, Q.; Ying, W. Study of the Fischer–Tropsch synthesis on nano-precipitated iron-based catalysts with different particle sizes. *RSC Adv.* **2020**, *10*, 42903–42911. [[CrossRef](#)]
60. Wu, X.; Qian, W.; Ma, H.; Zhang, H.; Liu, D.; Sun, Q.; Ying, W. Li-decorated Fe–Mn nanocatalyst for high-temperature Fischer–Tropsch synthesis of light olefins. *Fuel* **2019**, *257*, 116101. [[CrossRef](#)]
61. Xiong, H.; Motchelaho, M.A.; Moyo, M.; Jewell, L.L.; Coville, N.J. Effect of Group I alkali metal promoters on Fe/CNT catalysts in Fischer–Tropsch synthesis. *Fuel* **2015**, *150*, 687–696. [[CrossRef](#)]
62. Chen, Q.; Qian, W.; Zhang, H.; Ma, H.; Sun, Q.; Ying, W. Effect of Li promoter on FeMn/CNTs for light olefins from syngas. *Catal. Commun.* **2019**, *124*, 92–96. [[CrossRef](#)]
63. Qing, M.; Yang, Y.; Wu, B.; Wang, H.; Wang, H.; Xu, J.; Zhang, C.; Xiang, H.; Li, Y. Effect of the zirconia addition manner on the modification of Fe–SiO₂ interaction. *Catal. Today* **2012**, *183*, 79–87. [[CrossRef](#)]
64. Zhang, Y.; Wang, T.; Ma, L.; Shi, N.; Zhou, D.; Li, X. Promotional effects of Mn on SiO₂-encapsulated iron-based spindles for catalytic production of liquid hydrocarbons. *J. Catal.* **2017**, *350*, 41–47. [[CrossRef](#)]
65. Van Der Laan, G.P.; Beenackers, A.A.C.M. Kinetics and selectivity of the Fischer–Tropsch synthesis: A literature review. *Catal. Rev.* **1999**, *41*, 255–318. [[CrossRef](#)]
66. Xu, Y.; Li, X.; Gao, J.; Wang, J.; Ma, G.; Wen, X.; Yang, Y.; Li, Y.; Ding, M. A hydrophobic FeMn@Si catalyst increases olefins from syngas by suppressing C1 by-products. *Science* **2021**, *371*, 610–613. [[CrossRef](#)]
67. Zhu, Y.; Pan, X.; Jiao, F.; Li, J.; Yang, J.; Ding, M.; Han, Y.; Liu, Z.; Bao, X. Role of Manganese Oxide in Syngas Conversion to Light Olefins. *ACS Catal.* **2017**, *7*, 2800–2804. [[CrossRef](#)]

Disclaimer/Publisher’s Note: The statements, opinions and data contained in all publications are solely those of the individual author(s) and contributor(s) and not of MDPI and/or the editor(s). MDPI and/or the editor(s) disclaim responsibility for any injury to people or property resulting from any ideas, methods, instructions or products referred to in the content.